

2-nm-Thick NiCo LDH@NiSe Single-Crystal Nanorods Grown on Ni Foam as Integrated Electrode with Enhanced Areal Capacity for Supercapacitors

Chengxing Lu⁺^[a] Yu Yan⁺^[a] Tengfei Zhai,^[a] Yuzun Fan,^[a] and Wei Zhou^{*[a]}

It remains a great challenge to simultaneously guarantee the conductivity and high areal loading of active materials for integrated electrode of supercapacitors. Herein, we designed a hierarchical structure with cores of NiSe single-crystal nanorods and sheaths of 2-nm-thick NiCo thin sheets grown on nickel foam (NiCo LDH@NiSe/NF) as integrated electrode. It reaches a high areal capacity of $1131 \mu\text{Ah cm}^{-2}$ at a current density of 5 mA cm^{-2} , which is 2.2 times of NiSe/NF ($522 \mu\text{Ah cm}^{-2}$) and 6.0 times of NiCo LDH/NF ($189 \mu\text{Ah cm}^{-2}$), superior to most reported integrated electrodes. The enhanced areal capacity can be ascribed to the high active material loading of 6.5 mg cm^{-2} (twice more than other reported values) and

considerable conductivity of single-crystal NiSe nanorods of 2630 S cm^{-1} . The fabricated hierarchical integrated electrode of NiCo LDH@NiSe/NF assembled with activated carbon shows a maximum energy density of $0.454 \text{ mWh cm}^{-2}$ and a maximum power density of 80 mW cm^{-2} . This work presents supports of single-crystal nanorods for thin LDH sheets to fabricate high-density hierarchical structure for integrated electrode, which improves the conductivity and structural stability of active materials especially the LDHs, resulting in excellent electrochemical performance. It offers a promising approach to engineer and fabricate advanced supercapacitors with enhanced areal capacity.

1. Introduction

Supercapacitors (SCs), as one kind of efficient storage systems, have received wide attention due to their advantages of superior power density, safe operation, long life, and low maintenance cost.^[1–5] However, most commercialized SCs are symmetrical electrical double layer capacitors (EDLCs) of activated carbon (AC) as active materials, and their low energy density limits further applications.^[6] Recently, the battery-type materials (NiO, NiCoP, Ni_3Se_2 , etc) have received much more attention as the Faradaic charge storage and the diffusion-controlled nano-intercalation could obtain greater charge storage capacity.^[7–10] However, the areal mass loading of active materials in most literatures is generally limited within 3 mg cm^{-2} , resulting in a low areal capacity.^[11–14] Although the researchers can increase the areal loading intentionally, it might cause dramatic decrease in conductivity with dense aggregation of transitional metal compounds. Therefore, it is very important to improve the areal capacity by solving the problems between areal loading and conductivity. The simplest way is to grow active material directly on conductive substrate (nickel foam, carbon cloth, copper foam, etc) to serve

as an integrated electrode.^[8,15–17] As their high theoretical capacity and controllable layered structures, layered double hydroxides (LDHs) are chosen as one kind of promising battery-type active materials to grow for high capacity.^[18–22] They also face the shortcoming of poor conductivity, so the growing density of LDHs on conductive substrate needs to be controlled. For example, Nagaraju et al. prepared a binder-free NiCo LDH/Ni integrated electrode with NiCo LDH loading of $\sim 2.6 \text{ mg cm}^{-2}$, which showed a maximum areal capacity of $537 \mu\text{Ah cm}^{-2}$ at a current density of 2 mA cm^{-2} .^[12] Obviously, it remains a challenge to further increase the areal loading and simultaneously keep the conductivity for a higher areal capacity.

One-dimension (1D) nanowires or nanorods especially 1D single-crystal structures have unique electronic properties and structural advantages, which could promote the transfer of electrons from electrode surface to the substrate.^[23–26] Thus, the 1D single-crystal structures can be introduced to vertically grow on conductive substrate for secondary growth of LDHs. They can provide more spaces to increase the LDH loading and improve the conductivity of the formed hierarchical integrated electrode, even they can contribute partial capacity and increase the stability of the electrode. For example, Zhang et al. reported that single-crystal NiCo_2O_4 nanowires with fast electron transfer properties and strong mechanical strength showed high areal capacity of $520 \mu\text{Ah cm}^{-2}$ and 2000-cycle durability.^[27] Considering the component of 1D pillars, transition metal selenides might be a good choice as they have excellent electrochemical activity and excellent electrical conductivity (some reported valued can be up to $\sim 1.67 \times 10^4 \text{ S cm}^{-1}$) compared to transition metal oxides or sulfides.^[28–32] However, single-crystal transition metal selenides with high

[a] C. Lu,⁺ Y. Yan,⁺ T. Zhai, Dr. Y. Fan, Prof. Dr. W. Zhou
Beijing Advanced Innovation Center for Biomedical Engineering
School of Chemistry
Beihang University, Beijing 100191, China
E-mail: zhouwei@buaa.edu.cn

[+] These authors contributed equally to this work.

Supporting information for this article is available on the WWW under
<https://doi.org/10.1002/batt.201900215>

An invited contribution to a Special Collection dedicated to the Symposium on Batteries and Supercapacitors at the E-MRS Spring Meeting 2019

electrochemical activity and robust mechanical properties are rarely reported.

In this work, we firstly prepared robust single-crystal NiSe nanorod arrays by in-situ selenization of Ni foam (NF), and used them as electroactive inner core to support outer ultrathin NiCo LDH nanosheets, forming a multicomponent hierarchical core-sheath structure (NiCo LDH@NiSe/NF). This binder-free nanorod arrays have low contact resistance and short electronic transmission path. Under the support of these 1D arrays, the ultrathin NiCo LDH nanosheets (~ 2 nm) can successfully grow on them tightly and provides more active sites. This 3D core-sheath structure allows both NiSe core and NiCo LDH sheath to maximize participation in electrochemical processes. Remarkably, the obtained integrated NiCo LDH@NiSe/NF electrode exhibits a high areal capacity of $1131 \mu\text{Ah cm}^{-2}$ at a current density of 5 mA cm^{-2} along with good rate capability of 72% from 5 to 50 mA cm^{-2} with a high mass loading of 6.5 mg cm^{-2} . Our optimized hybrid supercapacitor (HSC) NiCo LDH@NiSe//AC delivers a high energy density of $0.454 \text{ mWh cm}^{-2}$ and high power density of 80 mW cm^{-2} along with excellent capacity retention of 91% even after 2000 cycles.

2. Results and Discussion

The fabrication process of hierarchical NiCo LDH@NiSe/NF is illustrated in Figure 1a. First, the single-crystal NiSe nanorod arrays were grown in-situ by a facile hydrothermal process utilizing NF and NaHSe as Ni and Se source, respectively. This in-situ self-supply Ni source avoids unevenness of the surface arrays and endows the arrays with robust mechanical properties, which can be used as scaffold to support secondary structures. Subsequently, these NiSe nanorods are wrapped by NiCo LDH ultrathin sheets through a controlled electrodeposition method.

Figures 1b-d show detailed morphology of the NF, NiSe/NF, and NiCo LDH@NiSe/NF by SEM images. The NF with high electrical conductivity of 3030 S cm^{-1} presents a 3D micro-porous framework (Figure 1b and Table 1), facilitating rapid internal infiltration of electrolyte and high mass loading of electroactive material. After selenization, the smooth surface of NF becomes rough (Figure S1). As shown in high-magnification SEM image of Figure 1c, the NiSe arrays on NF exhibit a homogeneous distribution over a large area. These nanorods are about 50 nm in diameter and $\sim 3 \mu\text{m}$ in length (Figure 1e). These 1D arrays provide rich sites for secondary growth of dense NiCo LDH nanosheets. Figure 1d shows that these NiCo LDH nanosheets homogeneously wrap the NiSe rods with crumpling and twisting structures. Notably, these wrapped rods are interconnected into three-dimension (3D) structure with porous structure. The cross-sectional SEM image of NiCo LDH@NiSe/NF in Figure 1f further reveals this 3D porous structure of NiSe nanorods are evenly wrapped by NiCo LDH nanosheets. As a contrast, the NiCo LDH nanosheets were completely covered on the surface of the NF without the aid of the NiSe arrays (Figure S2), forming NiCo LDH/NF. TEM image in Figure 1g further shows the NiCo LDH@NiSe core-sheath

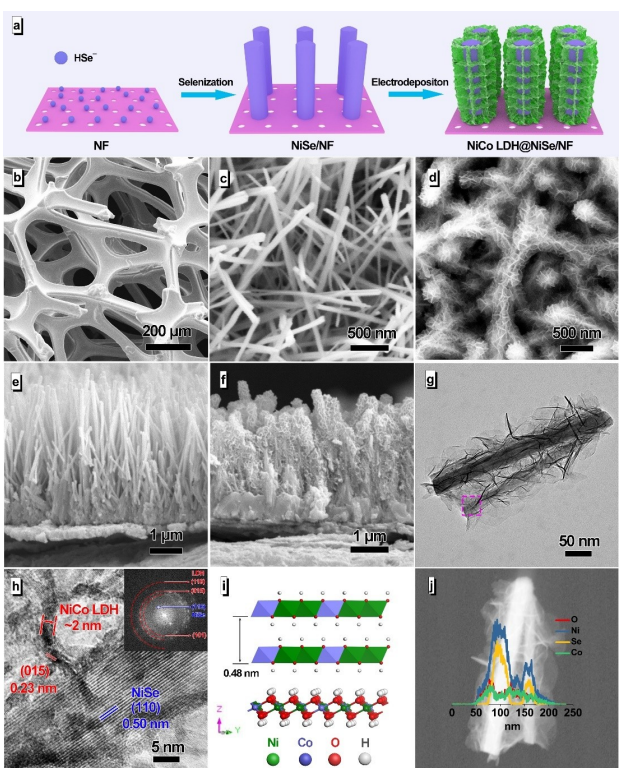


Figure 1. (a) Schematic illustration of the preparation of NiCo LDH@NiSe on Ni foam (NF). SEM images of the (b) Ni foam, (c) NiSe/NF, and (d) NiCo LDH@NiSe/NF. Cross-sectional SEM images of the (e) NiSe/NF and (f) NiCo LDH@NiSe/NF. (g) TEM and (h) HRTEM images of the NiCo LDH@NiSe, the inset is the corresponding FFT pattern. (i) Crystal structures of NiCo LDH, showing an interlayered thickness of 0.48 nm. (j) Dark-field scanning TEM image of NiCo LDH@NiSe with corresponding line-scanning results of O, Ni, Se, and Co elements.

Table 1. The electrical conductivity of the as-prepared materials.

| Samples | Electrical conductivity [S cm^{-1}] |
|------------------|--|
| NF | 3030 |
| NiSe/NF | 2630 |
| NiCo LDH@NiSe/NF | 2222 |
| NiCo LDH/NF | 1613 |

structure. The height of the outer wrapping layers is about 60 nm. In a typical HRTEM image in Figure 1h, the spacings from the lattice fringes of inner nanorod and outer nanosheet are about 0.5 and 0.23 nm, corresponding to the (110) planes of NiSe and the (015) planes of NiCo LDH. The corresponding fast Fourier transform (FFT) pattern (the inset of Figure 1h) further confirmed the existence of the (110) and (015) planes. In addition, the thickness of the outer NiCo LDH nanosheets is only ~ 2 nm, which can be solidly verified by the atomic force microscopy (AFM) result (Figure S3). As shown in Figure 1i, the crystallographic thickness of a single layer LDH is about 0.48 nm.^[33] It could be calculated that the outer LDHs have 4 atomic layers. Furthermore, the linear-scanning energy-dispersive X-ray spectroscopy (EDS) and elemental mapping analysis (Figure 1j and S4) show that the cores are Se and Ni elements while outer layers are Ni, Co and O elements, confirming the

hierarchical structure and multicomponent construction of the NiCo LDH@NiSe composite. The electrical conductivity of the as-prepared materials was tested by a four-point probe method, and the results are shown in Table 1. The NiSe/NF also shows a high conductivity of about 2630 S cm^{-1} , just a slight decrease compared with NF. It could be ascribed to a high conductivity of single-crystal NiSe. In addition, the conductivity of the NiCo LDH@NiSe/NF (2222 S cm^{-1}) is much higher than that of the NiCo LDH/NF (1613 S cm^{-1}). This shows that the construction of multicomponent hierarchical integrated electrode is beneficial to electron conduction.

The XRD patterns of the NiCo LDH, NiSe, and NiCo LDH@NiSe are shown in Figure 2a. The two strong peaks located at 44.5° and 51.9° marked by ♦ in the NiSe and NiCo LDH@NiSe are attributed to the planes of (111) and (200) of NF substrate (JCPDS NO. 70-0989). The other peaks at 2θ values of 17.7° , 31.0° , 34.1° , 38.7° and 46.5° can be ascribed to the planes of (110), (300), (021), (211) and (131) of NiSe (JCPDS NO. 18-0887). For the NiCo LDH@NiSe pattern, the weak diffraction peak at 11.3° , 22.7° , 33.5° , and 60.0° can be indexed to the (003), (006), (101), and (110) planes of the hydrotalcite-structured NiCo LDH (JCPDS: 38-0715).^[22] This confirms that the prepared sample is a composite of NiSe and NiCo LDH without other impurities. We further carried out the X-ray photoelectron spectroscopy (XPS) to identify chemical states and elements species of the NiCo LDH@NiSe/NF. The characteristic peaks for Ni, Co, Se, O, and C elements are displayed in the survey scan spectrum in Figure S5a. In the high-resolution XPS spectrum of Ni 2p (Figure 2b), there are two main spin-orbit doublets of Ni 2p_{3/2} and Ni 2p_{1/2} with the binding energies of 855.8 and 873.5 eV along with two shake-up satellite peaks centered at 861.5 and 879.7 eV. It indicates that the Ni species have +2 oxidation state in the prepared samples.^[34,35] The binding energies at 855.2 and 872.8 eV belong to metallic Ni 2p, corresponding to the NF substrate.^[36] Furthermore, the Co 2p

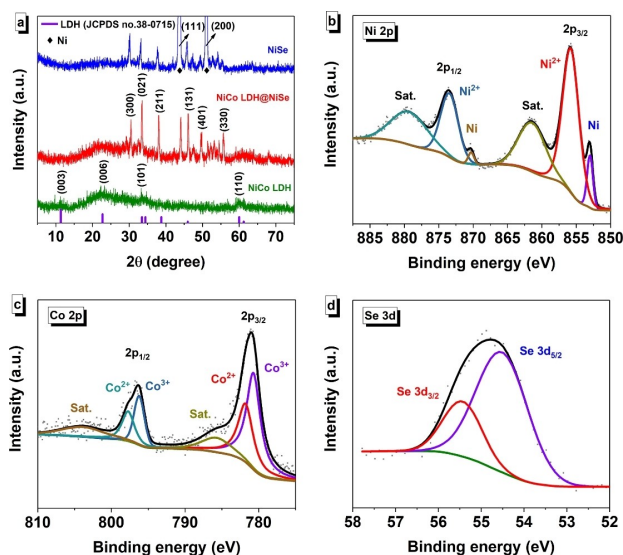


Figure 2. (a) XRD patterns of the NiCo LDH, NiSe, and NiCo LDH@NiSe. High-resolution XPS spectra of (b) Ni 2p, (c) Co 2p, and (d) Se 3d for NiCo LDH@NiSe/NF.

spectrum in Figure 2c can be well-fitted with two spin-orbit doublets, assigned to the presence of Co^{2+} and Co^{3+} . In the Se 3d spectrum (Figure 2d), the binding energies at 54.6 and 55.5 eV can well be ascribed to Se 3d_{5/2} and Se 3d_{3/2} in selenides with -2 valence.^[37] The O 1s spectrum (Figure S5b) exhibits two characteristic peaks at 532.5 and 531.1 eV corresponding to structural water ($\text{H}-\text{O}-\text{H}$) and metal-hydroxyl binding ($\text{Ni}-\text{OH}$ and $\text{Co}-\text{OH}$), respectively.^[22]

The electrochemical properties of the binder-free NiCo LDH@NiSe arrays as the working electrode was evaluated by a standard three-electrode system in 1 M KOH at room temperature. Figure 3a shows the comparative cyclic voltammetry (CV) curves of the NiCo LDH@NiSe/NF and its counterparts at a scan rate of 2 mV s^{-1} with the potential window from 0 to 0.7 V. For

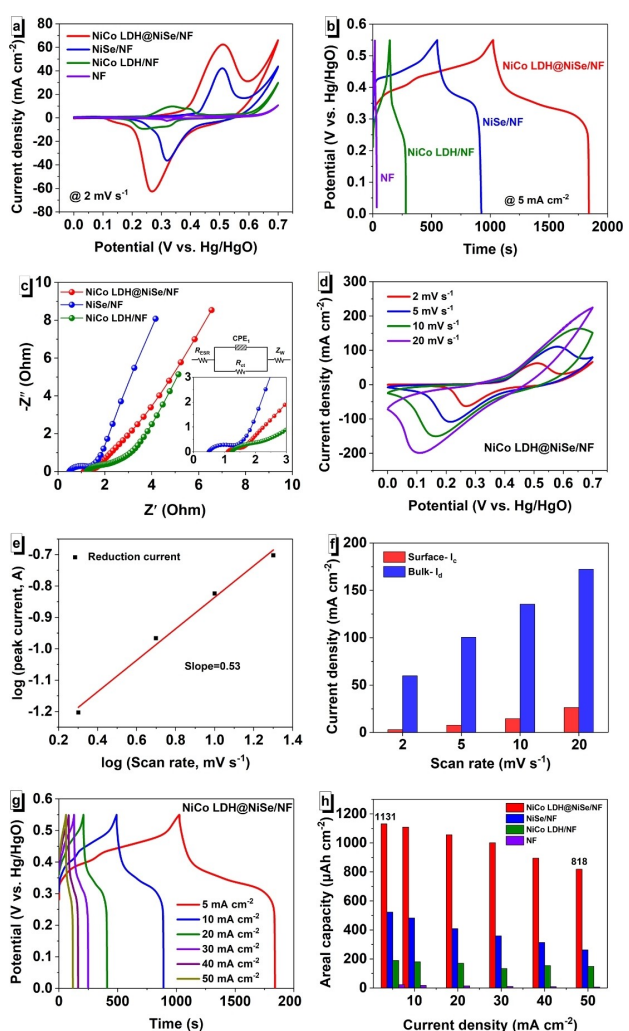


Figure 3. (a) Comparative CV curves and (b) GCD curves of the NiCo LDH/NF, NiSe/NF, and NiCo LDH@NiSe/NF. (c) Nyquist plots of EIS (the inset shows details in the high-frequency region and equivalent electric circuit model). (d) CV curves of the NiCo LDH@NiSe/NF electrode at various scan rates and current densities. (e) Calculated b-value of the reduction peak currents at scan rate of 2 to 20 mV s^{-1} of NiCo LDH@NiSe/NF electrode. (f) Calculated surface pseudocapacitive and bulk-insertion typed current density at various scan rates of NiCo LDH@NiSe/NF electrode. (g) GCD curves of the NiCo LDH@NiSe/NF electrode at various scan rates and current densities. (h) Calculated areal capacities of the NF, NiCo LDH/NF, NiSe/NF, and NiCo LDH@NiSe/NF.

pristine NF, the current response is extremely low, so the energy storage contribution is negligible. The CV profile of NiSe/NF clearly shows a pair of well-defined redox peaks (0.28–0.58 V vs. Hg/HgO), indicating a typical battery-type faradaic behavior of NiSe. The corresponding reversible faradaic reaction of NiSe can be logically established as [Eq. (1)]:^[39]



In the case of NiCo LDH@NiSe/NF, the voltage window of the redox peaks becomes wider (0.2–0.59 V vs. Hg/HgO) and the current response intensity become stronger, demonstrating the synergistic effect of NiCo LDH and NiSe. The additional involved electrochemical energy storage of outer NiCo LDH at 0.2–0.42 V vs. Hg/HgO were given below [Eqs. (2)–(3)]:^[39]



where M represents Ni or Co. In contrast, the NiCo LDH/NF exhibits a sluggish electrochemical behavior due to the 2D stacked nanosheets hindering electron transfer (Figure S2). The galvanostatic charge/discharge (GCD) curves of all samples at a current density of 5 mA cm⁻² are displayed in Figure 3b. As expected, the hierarchical NiCo LDH@NiSe/NF electrode displays a much larger discharge time (815 s) with a well-defined potential plateau, which further validates the enhanced electrochemical properties of multicomponent hierarchical electrodes through the decoration of NiCo LDH nanosheets. Meanwhile, the discharge times for the NiSe/NF, NiCo LDH/NF, and NF were only 377, 137, and 16 s, respectively. Furthermore, electrochemical impedance spectroscopy (EIS) analysis was carried out to identify the electrochemical conductivity of prepared electrodes. The Nyquist plots of all electrodes and equivalent electric circuit model are shown in Figure 3c. The intersection on the real axis at the high-frequency region is called equivalent series resistance (R_{ESR}), which is the sum of ionic resistance of the electrolyte, inherent resistance of the active material and contact resistance at the active material/collector interface.^[44] The diameter of the semicircle is closely related to the charge transfer resistance (R_{ct}) at the electrode material/electrolyte interface.^[40] The slightly tilted line at low-frequency region represents the Warburg resistance (Z_w), which is related to ion diffusion/migration in the electrolyte. Obviously, the NiCo LDH/NF shows the maximum R_{ESR} of 1.2 Ω and the maximum R_{ct} of 1.3 Ω, which is consistent with the previous conductivity results in the table. Compared with the R_{ESR} (0.5 Ω) and R_{ct} (0.9 Ω) of NiSe/NF, the addition of LDH nanosheets results in a larger R_{ESR} (1.1 Ω) and a lower R_{ct} (0.5 Ω) for NiCo LDH@NiSe/NF. This indicates that the multicomponent heterostructure electrode has better electrochemical activity and rapid faraday reaction occurring on the electrolyte/electrode interface.^[41]

Figures 3d and S6 show a series of CV curves of the NiCo LDH@NiSe/NF and other electrodes at various scan rates. All curves show a pair of visible cathodic and anodic peaks, which

indicates a battery-type Faradaic behavior and excellent electrochemical reversibility of the electrode material. In general, the peak currents in the CV curves subject to a power-law relationship with the scan rate [Eq. (4)]:^[42]

$$i = aV^b \quad (4)$$

where i is the peak current, V is the scan rate, a and b are the adjustable values. When $b=0.5$, it demonstrates an ideal semi-infinite linear diffusion-controlled process. When $b=1.0$, it indicates a surface induced capacitance process. As shown in Figure 3e, the b value was deduced from peaks in the cathodic reaction in Figure 3d, which was calculated to be 0.53 (the slope). This value represents a diffusion-controlled battery-type bulk mechanism in the present energy storage system. The contribution of battery-type bulk mechanism and surface pseudocapacitive mechanism can be determined by the following modified powers law [Eq. (5)]:^[43]

$$I_p = I_{\text{surface}} + I_{\text{bulk}} = C_{\text{surface}}V + C_{\text{bulk}}V^{1/2} \quad (5)$$

where I_p is the peak current density, V is the scan rate, C_{surface} and $C_{\text{bulk}}V^{1/2}$ correspond to the current contributions from the surface pseudocapacitive effect (I_{surface}) and battery-type bulk process (I_{bulk}), respectively.^[42,43] Figure 3f shows the contribution of current density from the surface pseudocapacitive and the battery-type bulk process at various scan rates. It can be seen that the battery-type bulk mechanism is dominant in the whole process.

The corresponding GCD curves of these samples at different current density are presented in Figures 3g and S7. These GCD curves exhibit a relatively symmetric shape, demonstrating the fast-faradaic reversibility of the prepared materials. According to the GCD curves of all samples, the values of calculated areal capacity at various current densities are shown in Figure 3h. The resulted values of NiCo LDH@NiSe/NF were 1131, 1108, 1056, 1001, 895, and 818 μAh cm⁻² at discharge current densities of 5, 10, 20, 30, 40, and 50 mA cm⁻², respectively, with an excellent rate capability of 72% (from 5 to 50 mA cm⁻²). When the current density is 5 mA cm⁻², the areal capacity of NiCo LDH@NiSe/NF is 2.2 times of NiSe/NF (522 μAh cm⁻²) and 6.0 times of NiCo LDH/NF (189 μAh cm⁻²). Even at each current density, the NiCo LDH@NiSe/NF electrode exhibited a maximum areal capacity. The corresponding energy storage performance of our integrated electrode also exceeds those of the previously reported electrodes, such as NiCo₂Al LDH (237 μAh cm⁻² at 0.8 mA cm⁻²),^[11] MnO₂@NiCo LDH/CoS₂ (473 μAh cm⁻² at 2 mA cm⁻²),^[14] NiCo₂S₄@NiCo LDH (631 μAh cm⁻² at 2 mA cm⁻²),^[44] Co₉S₈@PPy@NiCo LDH (368 μAh cm⁻² at 1 mA cm⁻²),^[45] and many other reports,^[12,13,46–49] as presented in Table S2. These excellent electrochemical properties of the NiCo LDH@NiSe/NF are mainly ascribed to the large mass loading, multicomponent synergy and accessible 3D porous network structure.

To explore the effect of different thicknesses of NiCo LDH on the electrochemical performance, we performed electrodeposition at different voltages. As shown in SEM image of

Figure S8a-b, the thickness of NiCo LDH at the applied voltage of 1.5 and 2.0 V is 12 and 20 nm, respectively. It shows that the thickness of NiCo LDH is positively related to the applied voltage. The GCD curves of NiCo LDH@NiSe/NF with different LDH thickness at a current density of 5 mA cm^{-2} are displayed in Figure S8c. It can be seen that the areal capacity decreases with the increase of LDH thickness, indicating that the ultrathin LDH is more favorable for the electrochemical reaction. In addition, as shown in Table S1, the 2-nm-thick LDH exhibits a higher conductivity and is more conducive to electron transport.

To further assess the application of the NiCo LDH@NiSe/NF electrode, a pouch-type hybrid supercapacitor was assembled with NiCo LDH@NiSe/NF as battery-type positive electrode and commercial AC coated NF (AC/NF) as double layer capacitive negative electrode. The electrochemical properties of the AC/NF electrode are shown in Figure S9 (Supporting Information). To achieve the maximum output of the HSCs, the mass loading of the positive and negative electrodes was optimized before assembling the device (more information is shown in Figure S10). Typically, the total operating potential of the HSCs has been considered as the sum of the voltages of the positive and negative electrodes. That is, the expected cell voltage is approximately 1.6 V, as shown in Figure 4a. To further determine the stable operating voltage of the HSC device with maximum charge storage, CV and GCD tests under various potential windows were performed. As shown in Figures 4b and 4c, we can observe the stable electrochemical potential window up to 1.6 V without any polarization. As the potential increases to 1.7 V, CV and GCD curves display a slight H_2/O_2 evolution accompanied by the decomposition of electrolyte.

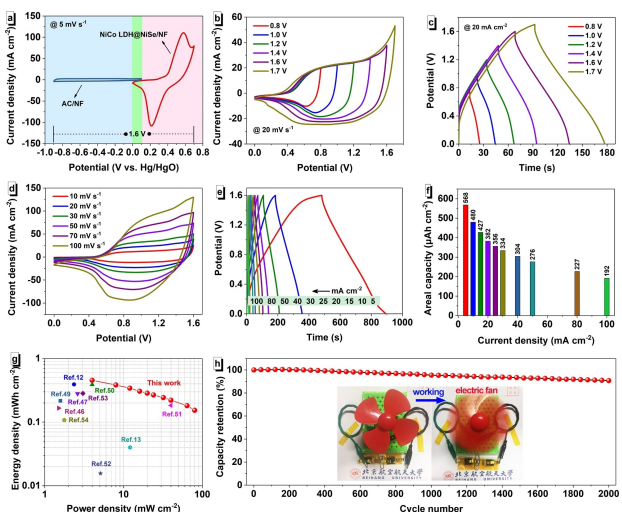


Figure 4. (a) CV curves of the NiCo LDH@NiSe and AC electrode in three-electrode system. (b) CV and (c) GCD plots of NiCo LDH@NiSe//AC HSCs obtained with different potential windows at a constant scan rate of 20 mV s^{-1} and current density of 20 mA cm^{-2} . (d) CV curves of the HSCs at various scan rates. (e) GCD curves of the HSCs at current densities from 5 to 100 mA cm^{-2} . (f) Calculated areal capacities vs. current density of the assembled HSCs. (g) Ragone plot of the assembled HSCs compared with some reported results. (h) Cycling stability of the HSC device at 20 mA cm^{-2} . The insets are the real-time applications of the electric fan using assembled HSC device (connected in series).

Thus, the voltage window of 0–1.6 V for CV curves of the HSC device as displayed in Figure 4d. The obtained CV shape is a combination of ideal capacitive and battery-type redox behavior. With the scan rate increasing from 10 to 100 mV s^{-1} , the shapes of CV curves mainly remain, demonstrating good reversibility and desirable rate capability. As shown in Figure 4e, the GCD curves of HSCs exhibit nearly symmetric charge-discharge time response at various current densities from 5 to 100 mA cm^{-2} , revealing an excellent Coulombic efficiency. Based on the discharge times, the calculated areal capacity values of HSC device at various current densities are shown in Figure 4f. The HSC device exhibits a maximum areal capacity of $568 \mu\text{Ah cm}^{-2}$ at an initial current density of 5 mA cm^{-2} , which can still maintain $192 \mu\text{Ah cm}^{-2}$ even at a high current density of 100 mA cm^{-2} . The areal energy and power densities of the HSCs were further calculated according to the discharge time and plotted in Figure 4g. The assembled HSC device delivers a maximum areal energy density of $0.454 \text{ mWh cm}^{-2}$ at a current density of 5 mA cm^{-2} with a power density of 4 mW cm^{-2} . Even at a higher current density of 100 mA cm^{-2} , the device still maintains an energy density of $0.153 \text{ mWh cm}^{-2}$ with a high power density of 80 mW cm^{-2} . Moreover, the areal energy and power densities of the assembled HSC device are higher than those of previously reported multicomponent hierarchical integrated electrode assembled HSCs (such as NiCo LDH//AC ($0.392 \text{ mWh cm}^{-2}$ at 2.4 mW cm^{-2}),^[12] NiCo LDH@Ag//AC (0.04 mWh cm^{-2} at 12.1 mW cm^{-2}),^[13] NiO@Co₃O₄-NiO//AC ($0.216 \text{ mWh cm}^{-2}$ at 1.58 mW cm^{-2}),^[49] and NiCo-H/rGO//AC (0.39 mWh cm^{-2} at 4 mW cm^{-2})^[50]) and even for the single-component integrated electrode assembled HSCs (such as Co@Co(OH)₂/carbon cloth ($0.166 \text{ mWh cm}^{-2}$ at 1.5 mW cm^{-2}),^[46] Cu_{1-x}Ni_x-O/Ni-P//porous carbon (0.28 mWh cm^{-2} at 2.6 mW cm^{-2}),^[47] Co₃O₄/GN//Bi₂O₃/GN ($0.183 \text{ mWh cm}^{-2}$ at 40 mW cm^{-2}),^[51] and Ni(OH)₂/Nb₂O₅ ($0.015 \text{ mWh cm}^{-2}$ at 5.1 mW cm^{-2})^[52]) and others slurry-coated electrode assembled HSCs (such as rGO/Ni-MOF//PPY ($0.283 \text{ mWh cm}^{-2}$ at 3 mW cm^{-2}),^[53] and NiCoMn-OH//RGO ($0.108 \text{ mWh cm}^{-2}$ at 1.8 mW cm^{-2})^[54]). As shown in Figure 4h, the long-term cycling stability of the assembled HSCs was also investigated at a high current density of 20 mA cm^{-2} . After 2000 cycles, the HSC device still keeps a good capacitance retention of 91%, indicating an excellent cycling stability. Figure S11 shows the corresponding SEM image of the electrode after 2000 cycles. The morphology of 1D NiSe rods wrapped by 2D NiCo LDH nanosheets mostly maintained. In addition, the surface of the material appears slightly rough due to the immersion in the electrolyte and the occurrence of the redox reaction. For further practical application, the two HSC devices connected in series successfully drive an electric fan (3 V), as shown in the inset of Figure 4h. Therefore, the assembled HSCs with well-designed hierarchical NiCo LDH@NiSe electrode might be a promising candidate for high-performance energy storage device.

3. Conclusions

In summary, we developed a hierarchical integrated electrode of NiCo LDH@NiSe/NF using single-crystal NiSe nanorods grown on nickel foam as high-conductivity scaffolding to support 2-nm-thick NiCo LDH nanosheets, forming a core-sheath structure. The robust single-crystal NiSe nanorods not only shows high conductivity (2630 S cm^{-1}), but also helps to shorten the electronic transport pathway. There are more active sites in few atomic layered LDHs, and the construction of 3D hierarchical structure facilitates electrolyte accessibility to the active sites. In addition, the multicomponent synergy provides a much-enhanced areal capacity compared with most reported LDH materials. Thus, the as-fabricated electrode can achieve a high areal capacity of $1131 \mu\text{Ah cm}^{-2}$ at a current density of 5 mA cm^{-2} , which is 2.2 times of NiSe/NF ($522 \mu\text{Ah cm}^{-2}$) and 6.0 times of NiCo LDH/NF ($189 \mu\text{Ah cm}^{-2}$), as well as a superior rate capability of 72% (from 5 to 50 mA cm^{-2}). Furthermore, the as-assembled HSC device of NiCo LDH@NiSe//AC delivers a high energy density of $0.454 \text{ mWh cm}^{-2}$ at the power density of 4 mW cm^{-2} , and an excellent cycling stability with a capacity retention of ~91% after 2000 cycles. Taking advantage of high energy density, the assembled HSC device can drive an electric fan, showing its potential suitability for practical applications.

Experimental Section

Growth of NiSe nanorod arrays on NF (NiSe/NF)

Typically, the NF substrates ($3 \times 2 \text{ cm}^2$) were etched by sonication in 3 M HCl solution for 5 min to remove the surface nickel oxide, and then rinsed with ethanol and deionized water multiple times. The NaHSe solution was prepared by dissolving 110 mg of Se powder in 6 mL of deionised (DI) water containing NaBH_4 (130 mg) and stirring for about 6 min until the solution was clear. Afterward, the prepared NaHSe solution was added into ethanol (34 mL) under N_2 flow. Then the solution was transferred into 50 mL Teflon-lined stainless-steel autoclave with a piece of pre-treated NF and the oven temperature was maintained at 140°C for 12 h. When the hydrothermal process was finished, the NF was taken out and cleaned with ethanol and DI water. After drying at 60°C in an oven for 12 hours, the NiSe nanorod arrays grown on the NF was successfully prepared. The mass loading of NiSe arrays on NF can be calculated as follows: $\text{NiSe}_{\text{loading}} = x \text{ mg} \times (M_{\text{NiSe}}/M_{\text{Se}}) = x \text{ mg} \times (138/79) = 1.7x \text{ mg}$. Where M is the molecular weight, x is the increased weight of NF after hydrothermal reaction. For NiSe/NF electrode, the loading mass of NiSe is calculated as $\sim 6 \text{ mg cm}^{-2}$. (Note: The source of Ni comes from NF, so the mass increase of NF after selenization is the mass of Se.)

Preparation of hierarchical NiCo LDH@NiSe/NF

The NiCo LDH nanosheets were prepared by an electrodeposition process with a three-electrode cell system. The as-prepared NiSe/NF (cut into pieces of $1 \times 1.5 \text{ cm}^2$, from which $1 \times 1 \text{ cm}^2$ area is employed for LDH growth) served as the working electrode, Ag/AgCl as a reference electrode, and platinum (Pt) wire as a counter electrode, respectively. Meanwhile, the electrodeposition solution was prepared by dissolving 13.2 mM of $\text{Co}(\text{NO}_3)_2 \cdot 6\text{H}_2\text{O}$ and 26.8 mM of $\text{Ni}(\text{NO}_3)_2 \cdot 6\text{H}_2\text{O}$ in 100 mL of DI water at room temper-

ature. Subsequently, the electrodeposition was applied at a potential of -1 V (vs Ag/AgCl) for 120 s, and then dried in a vacuum oven at 60°C . The mass loading of hierarchical NiCo LDH@NiSe on NF was about 6.5 mg cm^{-2} . For comparison, the NiCo LDH nanosheets were directly grown on pristine NF with the similar electrodeposition process.

Characterization

The morphologies and structures of the prepared samples were characterized by using a field-emission gun scanning electron microscope (SEM, Hitachi 7500) and a transmission electron microscopy (TEM, JEOL JEM-2200F). The X-ray diffraction patterns of the products were recorded by a Rigaku Dmax 2200 X-ray diffractometer with Cu-K α radiation ($\lambda = 1.5416 \text{ \AA}$). X-ray photoelectron spectroscopy measurements were performed on an ESCALAB 250 photoelectron spectrometer. The electrical conductivity of samples was measured by a standard four-point-probe resistivity measurement system (MCP-T610, Japan).

Electrochemical Measurements

All electrochemical properties (GCD, CV and EIS) were measured with a Gamry electrochemical workstation (Gamry Reference 600, Gamry Instruments, USA). The electrochemical performance of prepared samples was conducted in a conventional three-electrode system with a KOH (1 M) electrolyte, in which Hg/HgO electrode and platinum foil were used as reference and counter electrodes, respectively. The HSC was assembled with the NiCo LDH@NiSe/NF as a positive electrode, AC coated NF as a negative electrode, and a piece of nonwoven polypropylene membrane (NIKK-MPF30AC-100) soaked in 1 M KOH electrolyte as a separator. The sandwich assembly of this HSC was firmly packed by a Kapton tape. The areal capacity ($Q_{\text{act}} \text{ mAh cm}^{-2}$), energy density ($E, \text{ Wh cm}^{-2}$), and power density ($P, \text{ W cm}^{-2}$) values of the active materials in a three-electrode system and assembled HSCs can be calculated using the following equations [Eqs. (6)-(8)]:^[55]

$$Q = \frac{1}{1.8} \times \frac{\int_{t_i}^{t_f} V dt}{aU} \quad (6)$$

$$E = \frac{\int_0^t V_s dt}{3.6a} \quad (7)$$

$$P = \frac{3600 \times E}{t} \quad (8)$$

where I (A) is the discharge current, t (s) is the discharge time, t_i and t_f are the initial and final values of discharge time t (s), U (V) is the potential window, V_s (V) is the operating voltage, a (cm^2) is the active area of the electrode.

Acknowledgements

This work was financially supported by the National Natural Science Foundation of China (51472014 & 51972011).

Keywords: few layered NiCo LDH • integrated electrode • core-sheath structure • areal capacity • hybrid supercapacitor

- [1] N. Tuyen, M. d F Montemor, *Adv. Sci.* **2019**, *6*, 1801797.
- [2] J. Yan, S. Li, B. Lan, Y. Wu, P. S. Lee, *Adv. Funct. Mater.* **2019**, 1902564.
- [3] T. Qin, *Batteries & Supercaps* **2019**, *2*, 1.
- [4] Q. Xue, H. Gan, Y. Huang, M. Zhu, Z. Pei, H. Li, S. Deng, F. Liu, C. Zhi, *Adv. Energy Mater.* **2018**, *8*, 1703117.
- [5] Y. Lu, J. Liang, S. Deng, Q. He, S. Deng, Y. Hu, D. Wang, *Nano Energy* **2019**, *65*, 103993.
- [6] Z. Lin, E. Goikolea, A. Balducci, K. Naoi, P. L. Taberna, M. Salanne, G. Yushin, P. Simon, *Mater. Today* **2018**, *21*, 419.
- [7] Y. Lin, K. Sun, S. Liu, X. Chen, Y. Cheng, W. C. Cheong, Z. Chen, L. Zheng, J. Zhang, X. Li, Y. Pan, C. Chen, *Adv. Energy Mater.* **2019**, *9*, 1901213.
- [8] K. Tao, Y. Gong, J. Lin, *Nano Energy* **2019**, *55*, 65.
- [9] H. Luo, B. Wang, T. Liu, F. Jin, R. Liu, C. Xu, C. Wang, K. Ji, Y. Zhou, D. Wang, S. Dou, *Energy Storage Mater.* **2019**, *19*, 370.
- [10] C. Lu, A. Li, T. Zhai, C. Niu, H. Duan, L. Guo, W. Zhou, *Energy Storage Mater.* **2019**.
- [11] X. Gao, X. Liu, D. Wu, B. Qian, Z. Kou, Z. Pan, Y. Pang, L. Miao, J. Wang, *Adv. Funct. Mater.* **2019**, *29*, 1903879.
- [12] G. Nagaraju, S. Chandra Sekhar, L. Krishna Bharat, J. S. Yu, *ACS Nano* **2017**, *11*, 10860.
- [13] S. C. Sekhar, G. Nagaraju, J. S. Yu, *Nano Energy* **2017**, *36*, 58.
- [14] X. Wang, F. Huang, F. Rong, P. He, R. Que, S. P. Jiang, *J. Mater. Chem. A* **2019**, *7*, 12018.
- [15] F. Li, Y.-L. Liu, G.-G. Wang, H.-Y. Zhang, B. Zhang, G.-Z. Li, Z.-P. Wu, L.-Y. Dang, J.-C. Han, *J. Mater. Chem. A* **2019**, *7*, 22631.
- [16] P. Chang, H. Mei, Y. Zhao, W. Huang, S. Zhou, L. Cheng, *Adv. Funct. Mater.* **2019**, *29*, 1903588.
- [17] Y. Guo, X. Hong, Y. Wang, Q. Li, J. Mei, R. Dai, X. Liu, L. He, L. Mai, *Adv. Funct. Mater.* **2019**, *29*, 1809004.
- [18] X. Wang, H. Li, H. Li, S. Lin, J. Bai, J. Dai, C. Liang, X. Zhu, Y. Sun, S. Dou, *J. Mater. Chem. A* **2019**, *7*, 2291.
- [19] X. Li, D. Du, Y. Zhang, W. Xing, Q. Xue, Z. Yan, *J. Mater. Chem. A* **2017**, *5*, 15460.
- [20] W. Wang, Y. Lu, M. Zhao, R. Luo, Y. Yang, T. Peng, H. Yan, X. Liu, Y. Luo, *ACS Nano* **2019**, *13*, 12206.
- [21] Y. Jiang, Y. Song, Y. Li, W. Tian, Z. Pan, P. Yang, Y. Li, Q. Gu, L. Hu, *ACS Appl. Mater. Interfaces* **2017**, *9*, 37645.
- [22] K. Li, M. Liu, S. Li, F. Huang, L. Wang, H. Zhang, *J. Alloys Compd.* **2020**, *817*, 152712.
- [23] J. Jiang, Y. Li, J. Liu, X. J. N. Huang, *Nanoscale* **2011**, *3*, 45.
- [24] G. Zhou, L. Xu, G. Hu, L. Mai, Y. Cui, *Chem. Rev.* **2019**, *119*, 11042.
- [25] X. Xu, C. Cao, Y. J. E. A. Zhu, *Electrochim. Acta* **2015**, *155*, 257.
- [26] J. L. Xie, C. X. Guo, C. M. Li, *Energy Environ. Sci.* **2014**, *7*, 2559.
- [27] G. Q. Zhang, H. B. Wu, H. E. Hostler, M. B. Chan-Park, X. W. Lou, *Energy Environ. Sci.* **2012**, *5*, 9453.
- [28] C. Miao, P. Xu, J. Zhao, K. Zhu, K. Cheng, K. Ye, J. Yan, D. Cao, G. Wang, X. Zhang, *ACS Appl. Energy Mater.* **2019**, *2*, 3595.
- [29] Y. Tian, Y. Ruan, J. Zhang, Z. Yang, J. Jiang, C. Wang, *Electrochim. Acta* **2017**, *250*, 327.
- [30] P. Yang, Z. Wu, Y. Jiang, Z. Pan, W. Tian, L. Jiang, L. J. A. E. M. Hu, *Adv. Energy Mater.* **2018**, *8*, 1801392.
- [31] J. Theerthagiri, K. Karuppasamy, G. Durai, A. Rana, P. Arunachalam, K. Sangeetha, P. Kuppusami, H. S. Kim, *Nanomaterials* **2018**, *8*, 256.
- [32] C. Xia, Q. Jiang, C. Zhao, P. M. Beaujuge, H. N. Alshareef, *Nano Energy* **2016**, *24*, 78.
- [33] J. Zhao, S. Xu, K. Tschulik, R. G. Compton, M. Wei, D. O'Hare, D. G. Evans, X. Duan, *Adv. Funct. Mater.* **2015**, *25*, 2745.
- [34] X. Shi, J. Key, S. Ji, V. Linkov, F. Liu, H. Wang, H. Gai, R. Wang, *Small* **2019**, *15*, e1802861.
- [35] T. Wang, J. Wu, Y. Liu, X. Cui, P. Ding, J. Deng, C. Zha, E. Coy, Y. Li, *Energy Storage Mater.* **2019**, *16*, 24.
- [36] C. Tang, Z. Pu, Q. Liu, A. M. Asiri, X. Sun, Y. Luo, Y. He, *ChemElectroChem* **2015**, *2*, 1903.
- [37] X. Zhang, Y.-Y. Zhang, Y. Zhang, W.-J. Jiang, Q.-H. Zhang, Y.-G. Yang, L. Gu, J.-S. Hu, L.-J. Wan, *Small Methods* **2019**, *3*, 1800317.
- [38] H. Chen, M. Fan, C. Li, G. Tian, C. Lv, D. Chen, K. Shu, J. Jiang, *J. Power Sources* **2016**, *329*, 314.
- [39] H. C. Chen, Y. Qin, H. Cao, X. Song, C. Huang, H. Feng, X. S. Zhao, *Energy Storage Mater.* **2019**, *17*, 194.
- [40] Y. Chen, T. Zhou, L. Li, W. K. Pang, X. He, Y. N. Liu, Z. Guo, *ACS Nano* **2019**, *13*, 9376.
- [41] J. A. Syed, J. Ma, B. Zhu, S. Tang, X. Meng, *Adv. Energy Mater.* **2017**, *7*, 1701228.
- [42] Z. Wu, L. Jiang, W. Tian, Y. Wang, Y. Jiang, Q. Gu, L. Hu, *Adv. Energy Mater.* **2019**, *9*, 1900111.
- [43] Y. Yan, B. Hao, D. Wang, G. Chen, E. Markweg, A. Albrecht, P. Schaaf, *J. Mater. Chem. A* **2013**, *1*, 14507.
- [44] Y.-F. Wang, H.-T. Wang, S.-Y. Yang, Y. Yue, S.-W. J. A. a. m. Bian, *interfaces, ACS Appl. Mater. Interfaces* **2019**, *11*, 30384.
- [45] L. Wang, S. Li, F. Huang, X. Yu, M. Liu, H. Zhang, *J. Power Sources* **2019**, *439*, 227103.
- [46] C. Wan, Y. Jiao, D. Liang, Y. Wu, J. Li, *Adv. Energy Mater.* **2018**, *8*, 1802388.
- [47] G. Nagaraju, S. C. Sekhar, B. Ramulu, G. K. Veerasubramani, D. Narasimulu, S. K. Hussain, J. S. Yu, *Nano Energy* **2019**, *66*, 104054.
- [48] L. Ma, H. Fan, X. Wei, S. Chen, Q. Hu, Y. Liu, C. Zhi, W. Lu, J. A. Zapien, H. Huang, *J. Mater. Chem. A* **2018**, *6*, 19058.
- [49] S. Chandra Sekhar, G. Nagaraju, J. S. Yu, *Nano Energy* **2018**, *48*, 81.
- [50] J. Zhang, Z. Zheng, G. Wu, Q. Hua, *J. Alloys Compd.* **2019**, *785*, 725.
- [51] R. Liu, L. Ma, G. Niu, X. Li, E. Li, Y. Bai, G. Yuan, *Adv. Funct. Mater.* **2017**, *27*, 1701635.
- [52] X. Deng, Y. Jiang, Z. Wei, M. Mao, R. Pothu, H. Wang, C. Wang, J. Liu, J. Ma, *Green Energy & Environ.* **2019**, *4*, 382; *Environ.* **2019**, *4*, 382.
- [53] C. Cheng, J. Xu, W. Gao, S. Jiang, R. Guo, *Electrochim. Acta* **2019**, *318*, 23.
- [54] Y. Zhu, C. Huang, C. Li, M. Fan, K. Shu, H. C. Chen, *J. Power Sources* **2019**, *412*, 559.
- [55] S. Liu, Y. Yin, D. Ni, K. S. Hui, M. Ma, S. Park, K. N. Hui, C. Y. Ouyang, S. C. Jun, *Energy Storage Mater.* **2019**, *22*, 384.

Manuscript received: December 12, 2019
Revised manuscript received: January 22, 2020
Accepted manuscript online: February 3, 2020
Version of record online: February 11, 2020